

Vortex Lattice Formation in Spin–Orbit-Coupled Spin-2 Bose–Einstein Condensate Under Rotation

Paramjeet Banger

Department of Physics, Indian Institute of Technology Ropar,
Rupnagar 140001, Punjab, India.

Corresponding author(s). E-mail(s): 2018phz0003@iitrpr.ac.in;

Abstract

We investigate the vortex-lattice configuration in a rotating spin orbit-coupled spin-2 Bose-Einstein condensate confined in a quasi-two-dimensional harmonic trap. By considering the interplay between rotation frequency, spin-orbit couplings, and interatomic interactions, we explore a variety of vortex-lattice structures emerging as a ground-state solution. Our study focuses on the combined effects of spin-orbit coupling and rotation, analysed by using the variational method for single-particle Hamiltonian. We observe that the interplay between rotation and Rashba spin-orbit coupling gives rise to different effective potentials for the bosons. Specifically, at higher rotation frequencies, isotropic spin-orbit coupling leads to an effective toroidal potential, while fully anisotropic spin-orbit coupling results in a symmetric double well potential. To obtain these findings, we solve the five coupled Gross-Pitaevskii equations for the spin-2 BEC with spin-orbit coupling under rotation. Notably, we find that the antiferromagnetic, cyclic, and ferromagnetic phases exhibit similar behavior at higher rotation.

Keywords: Spin-2 BECs, Spin-orbit coupling, Rotation, Vortex-lattice

1 Introduction

In recent decades, advancements in optical traps within cold atom experiments have facilitated investigations into spinor Bose–Einstein condensates (BECs).

The experimental realization of spin-orbit (SO) coupling in spinor BECs has been one of the most important advancements in the last decade [1], thus opening up avenues for numerous novel studies on spin-2 BECs [2, 3]. Spin-2 BECs with SO coupling have also been proposed theoretically [4]. In SO-coupled spinor BEC, exotic vortex-lattice configuration has been explored in the presence of rotation [5]. The combined effect of both SO coupling and rotation frequency facilitates the emergence of a variety of topological configurations in pseudospin BEC [5–10]. The interplay of isotropic SO coupling and rotation resulting in the emergence of half-skyrmion excitations in rotating and rapidly quenched spin-1 BECs using stochastic projected Gross-Pitaevskii equations have been studied in [11–15]. Rotating spin-1 BEC also supports many interesting solutions in the presence of an isotropic [13, 16] as well as anisotropic, [11, 12, 16] SO coupling. Moreover, numerical studies on rotating SO-coupled BEC has been done in toroidal traps [14], with Weyl SO coupling [15], and SU(3) coupling [17]. Recently, by considering the isotropic SO-coupled spin-2 BEC under rotation topological vortical phase transitions have been studied theoretically [18]. This numerical study has been done for small to moderate rotation frequency. However, SO-coupled spin-2 BECs systems have not been completely investigated. In this work we fully examine anisotropic as well as isotropic SO-coupling with moderate to higher rotation frequencies. We investigate a quasi-two-dimensional (q2D) harmonically trapped spin-2 condensate, featuring an anisotropic SO-coupling term proportional to $S_x \hat{p}_x$, as well as an isotropic SO coupling term proportional to $(S_x \hat{p}_y - S_y \hat{p}_x)$. We choose ^{23}Na [19], ^{87}Rb [20], and ^{83}Rb [19] BECs as the prototypical examples of systems with antiferromagnetic, cyclic, and ferromagnetic spin-exchange interactions. We compute the rotational energy per particle as a function of rotation frequency, and at higher rotation, antiferromagnetic, cyclic, and ferromagnetic phases exhibit qualitatively similar behavior. To analyze the characteristics of the SO-coupled non-interacting Hamiltonian under rotation, we employed a variational method. During the investigation of the single-particle Hamiltonian, we interpret the effective potentials experienced by bosons. The detailing of calculating effective potentials for SO-coupled spin-2 BEC under rotation is discussed in Appendix. The paper is as follows. In Section 2, we use a variational method to study the properties of the non-interacting Hamiltonian and interpret the effective potential experienced by bosons in the presence of rotation and SO coupling. In Section 3, we introduce formalism of the mean-field model for an SO-coupled spin-2 BEC in the rotating frame and discuss the Coupled Gross pitiaevskii Equations (CGPEs). The Numerical results of the interacting systems are discussed in Section 4. Finally, in Section 5, we conclude the results of our study.

2 Single particle Analysis

In our study, we examine a spin-2 BEC with SO coupling that is confined in the xy -plane. The condensate is subjected to a q2D harmonic trap of the form

$m(\omega_x^2 x^2 + \omega_y^2 y^2 + \omega_z^2 z^2)/2$, where ω_z is significantly larger than $\omega (= \omega_x = \omega_y)$ along the z -direction. The single particle Hamiltonian for an SO-coupled spin-2 BEC in rotating frame can be described as [6, 21, 22]

$$H = H_{\text{lab}} - \Omega L_z \quad (1)$$

where Ω is the angular frequency of rotation, $L_z = -i(x\partial/\partial y - y\partial/\partial x)$ is the z component of the angular momentum operator, and H_{lab} is single particle laboratory frame Hamiltonian, can be written in the dimensionless form

$$H_{\text{lab}} = \left(\frac{\hat{p}_x^2 + \hat{p}_y^2}{2} + \frac{x^2 + y^2}{2} \right) \times \mathbf{1} + H_{\text{SOC}}, \quad (2)$$

where $\mathbf{1}$ represents a 5×5 identity matrix, and $\hat{p}_d = -i\partial/\partial d$ with $d = x, y$. The H_{SOC} can be expressed as *case I*: $\gamma_x S_x \hat{p}_x$ experimentally achievable equal-strength mixture of Rashba and Dresselhaus couplings [1] terming as an anisotropic spin-orbit coupling for q2D-system. Alternatively, *case II*: $\gamma(S_x \hat{p}_y - S_y \hat{p}_x)$, which represents the Rashba spin-orbit coupling [23] between the spin and the linear momentum along the xy -plane. The γ_x and γ are the SO coupling strength for respective cases. S_d is the irreducible representations of the d -component of angular momentum operators for spin-2 matrix with $d = x, y$.

$$(S_x)_{j',j} = \frac{1}{2} \left(\sqrt{(6-j'j)} \hbar \delta_{j',j+1} + \sqrt{6-j'j} \hbar \delta_{j'+1,j} \right), \quad (3)$$

$$(S_y)_{j',j} = \frac{1}{2i} \left(\sqrt{(6-j'j)} \hbar \delta_{j',j+1} - \sqrt{(6-j'j)} \hbar \delta_{j'+1,j} \right). \quad (4)$$

with j' and j varies from -2 to 2 . To describe the combined effect of rotation and spin-orbit coupling, we analyse the single particle Hamiltonian. To examine the Eq. (1) for *case I* we consider the following normalized variational *ansatz*

$$\Psi_{\text{var}}^{\pm} = \frac{\exp \left[-\frac{(x-x_0)^2}{2} - \frac{(y-y_0)^2}{2} + i(k_x x + k_y y) \right]}{2\sqrt{\pi}} \times \left(\frac{1}{4}, \mp \frac{1}{2}, \sqrt{\frac{3}{8}}, \mp \frac{1}{2}, \frac{1}{4} \right)^T, \quad (5)$$

where x_0, y_0, k_x and k_y are the variational parameters. The variational energies are

$$E_{\text{var}}^{\pm}(x_0, y_0, k_x, k_y) = \int dx dy \Psi_{\text{var}}^{\pm *} H \Psi_{\text{var}}^{\pm},$$

4 Vortex-lattice formation in SO-coupled spin-2 BEC under rotation

$$\begin{aligned}
&= \frac{1}{2} [k_x(\mp 4\gamma_x + k_x + 2\Omega y_0) + k_y^2 \\
&\quad - 2k_y x_0 \Omega + x_0^2 + y_0^2 + 2], \tag{6a}
\end{aligned}$$

where $\Psi_{\text{var}}^{\pm*}$ is the conjugate transpose of Ψ_{var}^{\pm} . The variational parameters can be fixed by minimizing E_{var}^{\pm} with respect to (x_0, y_0, k_x, k_y) . The location(s) of minima thus obtained are

$$x_0 = 0, \quad y_0 = \mp \frac{2\gamma_x \Omega}{1 - \Omega^2}, \quad k_x = \pm \frac{2\gamma_x}{1 - \Omega^2}, \quad k_y = 0, \tag{7}$$

$$E_{\text{min}}^{\pm} = \frac{2\gamma_x^2 + \Omega^2 - 1}{\Omega^2 - 1}, \tag{8}$$

for Ψ_{var}^{\pm} . The most generic variational solution for these parameters' sets is $c_+ \Psi_{\text{var}}^+ + c_- \Psi_{\text{var}}^-$, where c_{\pm} are coefficients of superposition with $|c_+|^2 + |c_-|^2 = 1$. The resultant density profile reflects the effective two-well potentials with two minima at $(x_0 = 0, y_0 = \mp 2\gamma_x \Omega / (1 - \Omega^2))$. The validity of the variational method has been checked by considering the set of parameter (γ_x, Ω) is $(1, 0.5)$, $(1, 0.7)$, and $(1, 0.9)$. For these parameters set, the variational solutions Ψ_{var}^{\pm} are degenerate, and the peak of total variational densities lies at ± 1.33 , ± 2.74 , ± 9.47 , respectively. The densities profiles obtained by the variational method for non-interacting systems are in excellent agreement with the numerical results (not shown here) and so as the corresponding energies. The rotating spin-2 BEC in the presence of anisotropic SO-coupling is exactly solvable [16]. The ansatz presented here is an exact analytic solution to a one-dimensional SO coupling Hamiltonian under rotation.

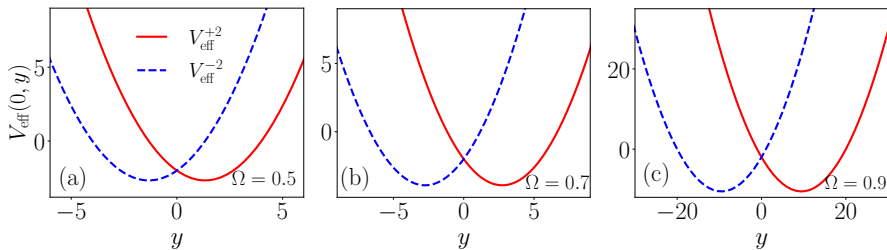


Fig. 1 (Color online) (a)-(c) are the curves of effective potentials corresponding to Eq. (22) for $\Omega_{\text{rot}} = 0.5, 0.7$ and 0.9 , respectively. For these curves, SO-coupling strength is $\gamma_x = 1$.

The effective potential incurred by the boson can be evaluated by calculating the vector and scalar potentials as discussed in ref. [6, 16]. With the definition given in [6], the effective potential for rotating SO-coupled spin-2 system calculated in Appendix. The effective potential curves for the system are

$$V_{\text{eff}}^j(x, y) = \frac{1}{2} [(1 - \Omega^2)(x^2 + y^2) - j^2 \gamma_x^2 - 2j\gamma_x \Omega y]. \tag{9}$$

where $j = \pm 2, \pm 1, 0$. The minima of effective potential occurred in the curves corresponding to $j = \pm 2$ depending on the region of $y > 0$ or $y < 0$, respectively illustrated in Fig. 1. Eq. (9) exhibiting that $V_{\text{eff}}^{+2}(x, y)$ and $V_{\text{eff}}^{-2}(x, y)$ are overlap at $(x = 0, y = 0)$ as shown in Fig. 1. In the region $y < 0$, V_{eff}^{-2} corresponding to $j = -2$ curve is lower than other for $j = 0, \pm 1, +2$ (curves for $j = 0, \pm 1$ are not shown here) and in $y > 0$, V_{eff}^{+2} which is corresponding to $j = +2$ is lower than the other curves for $j = 0, \pm 1, -2$. Fig. 1(a)-(c) show the effective potential curves for rotation frequencies $\Omega = 0.5, 0.7$ and 0.9 , respectively. The potentials incurred by boson are effectively equivalent to symmetric double-well potentials with minima exhibit at $(x = 0, y = \mp 1.33)$, $(x = 0, y = \mp 2.74)$, and $(x = 0, y = \mp 9.47)$ for $\Omega = 0.5, 0.7$ and 0.9 , respectively.

In order to investigate the system with isotropic SO coupling, we consider the following variational *ansatz*

$$\Phi_{\text{var}} = \frac{\exp\left(\frac{r^2}{2\sigma^2}\right)}{\sqrt{\pi\sigma^{2n+4}\Gamma(n+2)}} \times (A_1 r^{|n|} e^{in\phi}, A_2 r^{|n+1|} e^{i(n+1)\phi}, A_3 r^{|n+2|} e^{i(n+2)\phi}, \\ A_4 r^{|n+3|} e^{i(n+3)\phi}, A_5 r^{|n+4|} e^{i(n+4)\phi})^T, \quad (10)$$

where, the variational amplitudes are denoted as A_1, A_2, A_3, A_4, A_5 , while σ represents the variational width of the ansatz, and n is a variational integer. The normalization condition imposes the constraint

$$(n+2)\sigma^2 ((n+3)\sigma^2 (A_5^2(n+4)\sigma^2 + A_4^2) + A_3^2) + A_2^2 + \frac{A_1^2}{(n+1)\sigma^2} = 1, \quad (11)$$

on the variational parameters $A_1, A_2, A_3, A_4, A_5, n$ and σ . The variational energy is

$$E_{\text{var}}(A_1, A_2, A_3, A_4, A_5, n, \sigma) = [4A_1 A_2 \gamma (n+1)\sigma^2 + (n+1)\sigma^2 (2\sqrt{6}A_2 A_3 \gamma (n+2)\sigma^2 \\ + (n+2)\sigma^2 (2\sqrt{6}A_3 A_4 \gamma (n+3)\sigma^2 + (n+3)\sigma^2 (4A_4 A_5 \gamma (n+4)\sigma^2 + A_5^2 (n+4)\sigma^2 ((n+5) \\ (\sigma^4 + 1) - 2(n+4)\sigma^2 \Omega) + A_4^2 ((n+4)(\sigma^4 + 1) - 2(n+3)\sigma^2 \Omega)) + A_3^2 ((n+3)(\sigma^4 + 1) - \\ 2(n+2)\sigma^2 \Omega) + A_2^2 ((n+2)(\sigma^4 + 1) - 2(n+1)\sigma^2 \Omega) + A_1^2 ((n+1)(\sigma^4 + 1) \\ - 2n\sigma^2 \Omega)] / (2(n+1)\sigma^4) \quad (12)$$

The variational energy can be minimized with all variational parameters subjected to the constraint specified in Eq (11), to decide the variational parameters. To check the validity of the variational method in this case, we choose ($\gamma = 1, \Omega = 0.9$), the variational parameters while minimization of (12) are $(A_1, A_2, A_3, A_4, A_5, n, \sigma) = (-2.3728, 0.5012, -0.0645, 0.0055, -0.0002, 98, 0.9491)$. The comparison of variational density $|\Phi_{\text{var}}(r)|^2$, and exact numerically evaluated single particle

density profiles $|\Psi(r)|^2$, agree with each other. The peak of total variational density lies along a circle of radius 9.47 and is related to the effective toroidal potential incurred by the boson. For $(\gamma = 1, \Omega = 0.7)$ the variational parameters while minimization are variational energy $(A_1, A_2, A_3, A_4, A_5, n, \sigma) = (0.7029, -0.5115, 0.2173, -0.0589, 0.0094, 9, 0.8489)$ for parameters' sets, respectively. The comparison of $|\Phi_{\text{var}}(r)|^2$, and $|\Psi(r)|^2$, agree with each other and the peak of total variational density lies along a circle of radius 2.70.

3 Mean-field interacting Model

In q2D trapping potential, a rotating SO-coupled spin-2 BEC under mean-field approximation can be described by a set of five CGPEs [21]

$$i \frac{\partial \phi_{\pm 2}}{\partial t} = \mathcal{H} \phi_{\pm 2} + c_0 \rho \phi_{\pm 2} + c_1 \{F_{\mp} \phi_{\pm 1} \pm 2F_z \phi_{\pm 2}\} + c_2 \frac{\Theta \phi_{\mp 2}^*}{\sqrt{5}} + \Gamma_{\pm 2} \quad (13a)$$

$$i \frac{\partial \phi_{\pm 1}}{\partial t} = \mathcal{H} \phi_{\pm 1} + c_0 \rho \phi_{\pm 1} + c_1 \left(\sqrt{\frac{3}{2}} F_{\mp} \phi_0 + F_{\pm} \phi_{\pm 2} \pm F_z \phi_{\pm 1} \right) - c_2 \frac{\Theta \phi_{\mp 1}^*}{\sqrt{5}} + \Gamma_{\pm 1}, \quad (13b)$$

$$i \frac{\partial \phi_0}{\partial t} = \mathcal{H} \phi_0 + c_0 \rho \phi_0 + c_1 \sqrt{\frac{3}{2}} \{F_- \phi_{-1} + F_+ \phi_1\} + c_2 \frac{\Theta \phi_0^*}{\sqrt{5}} + \Gamma_0, \quad (13c)$$

where, $\Phi = (\phi_2, \phi_1, \phi_0, \phi_{-1}, \phi_{-2})^T$ is a five component order parameter,

$$\mathcal{H} = -\frac{\nabla^2}{2} + V - \Omega L_z, \quad \Theta = \frac{2\phi_2 \phi_{-2} - 2\phi_1 \phi_{-1} + \phi_0^2}{\sqrt{5}}, \quad F_z = \sum_{j=-2}^2 j |\phi_j|^2$$

$$F_- = F_+^* = 2\phi_{-2}^* \phi_{-1} + \sqrt{6} \phi_{-1}^* \phi_0 + \sqrt{6} \phi_0^* \phi_1 + 2\phi_2 \phi_1^*,$$

and $\rho = \sum_{j=-2}^2 |\phi_j|^2$ is the total density. The Laplacian, trapping potential V , interaction parameters (c_0, c_1, c_2) , are defined as

$$\nabla^2 = \left(\frac{\partial}{\partial x^2} + \frac{\partial}{\partial y^2} \right), \quad V = \frac{x^2 + y^2}{2}, \quad c_0 = \sqrt{2\pi\alpha_z} \frac{2\pi N(4a_2 + 3a_4)}{7a_{\text{osc}}}, \quad (14a)$$

$$c_1 = \sqrt{2\pi\alpha_z} \frac{2\pi N(a_4 - a_2)}{7a_{\text{osc}}}, \quad c_2 = \sqrt{2\pi\alpha_z} \frac{2\pi N(7a_0 - 10a_2 + 3a_4)}{7a_{\text{osc}}}, \quad (14b)$$

and the Γ 's for *case I* are

$$\Gamma_{\pm 2} = -i\gamma_x \frac{\partial \phi_{\pm 1}}{\partial x}, \quad \Gamma_{\pm 1} = -i \left(\gamma_x \frac{\partial \phi_{\pm 2}}{\partial x} + \sqrt{\frac{3}{2}} \gamma_x \frac{\partial \phi_0}{\partial x} \right),$$

$$\Gamma_0 = -i \left(\sqrt{\frac{3}{2}} \gamma_x \frac{\partial \phi_1}{\partial x} + \sqrt{\frac{3}{2}} \gamma_x \frac{\partial \phi_{-1}}{\partial x} \right),$$

for case II are

$$\begin{aligned} \Gamma_{\pm 2} &= -i\gamma \left(\frac{\partial \phi_{\pm 1}}{\partial y} \pm i \frac{\partial \phi_{\pm 1}}{\partial x} \right), \\ \Gamma_{\pm 1} &= -i\gamma \left(\frac{\partial \phi_{\pm 2}}{\partial y} + \sqrt{\frac{3}{2}} \frac{\partial \phi_0}{\partial y} \mp i \frac{\partial \phi_{\pm 2}}{\partial x} \pm i \sqrt{\frac{3}{2}} \frac{\partial \phi_0}{\partial x} \right), \\ \Gamma_0 &= -i\gamma \left(\sqrt{\frac{3}{2}} \frac{\partial \phi_1}{\partial y} + \sqrt{\frac{3}{2}} \frac{\partial \phi_{-1}}{\partial y} - i \sqrt{\frac{3}{2}} \frac{\partial \phi_1}{\partial x} + i \sqrt{\frac{3}{2}} \frac{\partial \phi_{-1}}{\partial x} \right). \end{aligned}$$

where a_0, a_2, a_4 represent the s -wave scattering lengths in the allowed scattering channels, and α_x, α_y and α_z are the anisotropy parameters of trapping frequency. All these quantities are dimensionless, which have been calculated by expressing lengths (a_0, a_2, a_4, x, y) in units of $a_{\text{osc}} \equiv \sqrt{\hbar m / \omega}$, energy, density and time in the unit of $\hbar\omega$, a_{osc}^{-2} , and ω^{-1} , respectively. The dimensionless form of the mean-field model for the SO-coupled spin-2 has two conserved quantities: one is the normalization condition $\int \rho(x, y) dx dy = 1$. And the other is energy per particle defined as

$$E = \int dx dy \left[\sum_{j=-2}^{+2} \phi_j^* \mathcal{H} \phi_j + \frac{c_0}{2} \rho^2 + \frac{c_1}{2} |\mathbf{F}|^2 + \frac{c_2}{2} |\Theta|^2 + \sum_{j=-2}^{+2} \phi_j^* \Gamma_j \right], \quad (17)$$

for an SO-coupled BEC. Under the influence of SO coupling longitudinal magnetization

$$\mathcal{M} = \int (2|\phi_{+2}|^2 + |\phi_{+1}|^2 - |\phi_{-1}|^2 - 2|\phi_{-2}|^2) dx dy, \quad (18)$$

is not conserved, although it remain conserved for $\gamma_x = 0$ and $\gamma = 0$.

4 Numerical Results

We take a typical example of antiferromagnetic system trapped in a q2D potential, consisting of 50,000 atoms of an SO-coupled ^{23}Na spin-2 BECs with $\omega = 2\pi \times 10$ Hz, $\omega_z = 2\pi \times 100$ Hz, and so $\alpha_x = \alpha_y = 1$ and $\alpha_z = 10$ where $\alpha_\nu = \omega_\nu / \omega_x$. The three scattering lengths considered for this system are $a_0 = 34.9a_B, a_2 = 45.8a_B, a_4 = 64.5a_B$ [19] and corresponding triplet of dimensionless interaction strengths are $(c_0, c_1, c_2) = (340.45, 16.90, -18.25)$. The oscillator length for this system is $4.69\mu\text{m}$. For the cyclic phase, we examine a system composed of 50,000 atoms of ^{87}Rb spin-2 BECs confined in a q2D trapping potential with the same trapping frequencies considered for anti-ferromagnetic phase. The chosen triplet of scattering lengths for this system

8 Vortex-lattice formation in SO-coupled spin-2 BEC under rotation

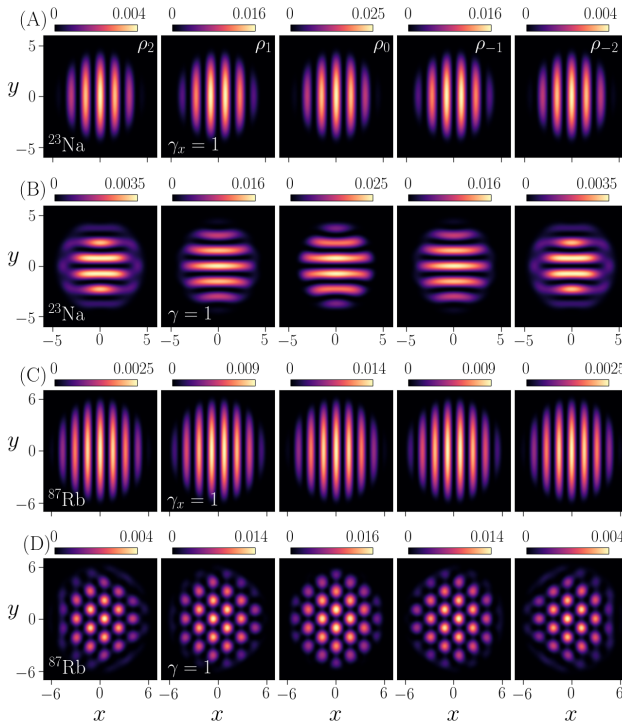


Fig. 2 (Color online) (A) and (B) shown the ground state component densities for an anisotropic SO coupling and isotropic SO-coupling ^{23}Na spin-2 BEC, respectively. The interaction parameters for both cases are $c_0 = 340.45$, $c_1 = 16.90$, $c_2 = -18.25$, and SO coupling strength for (A) $\gamma_x = 1$ and (B) $\gamma = 1$. Similarly, (C) and (D) represent the same for ^{87}Rb spin-2 BEC for interaction parameters $c_0 = 1164.80$, $c_1 = 13.88$, $c_2 = 0.43$.

consists of $a_0 = 87.93a_B$, $a_2 = 91.28a_B$, and $a_4 = 99.18a_B$ [20], resulting in the corresponding dimensionless interaction strengths of $(c_0, c_1, c_2) = (1164.80, 13.88, 0.43)$. The oscillator length in this system is $2.41\mu\text{m}$.

We investigate the stationary state solutions of these systems in the presence SO coupling. To solve the set of CGPEs in (13a)-(13c), we employ the time-splitting Fourier spectral method [24–27]. To obtain the numerical solutions, a spatial step size of 0.1 and a temporal step size of 0.001 to be used. In the absence of a rotation frequency ($\Omega = 0$), the equations are evolved in imaginary time propagation to obtain the ground state of the system. Multiple numerical simulations are performed with different initial guesses, and the state with the lowest energy is considered as the ground state solution. When $\Omega = 0$, the spin-2 BEC can exhibit various ground state solutions depending on the interaction parameters and the strength of the spin-orbit coupling. The most general solution is axisymmetric, characterized by $(-2, -1, 0, +1, +2)$ phase singularities at densities corresponding to $j = +2, +1, 0, -1, -2$ components [28]. Additionally, other patterns such as stripes [28], square lattices

[28], or triangular lattices [28] can arise through the superposition of counter-propagating plane waves, four plane waves with propagation vectors at a right angle to each other, or three plane waves with propagation vectors at an angle of $2\pi/3$ to each other, respectively. When performing simulation in a rotating frame, previously obtained ground state solutions are considered as an initial guess. The dynamical stability of each solution has been studied through real-time propagation, with the converged solution obtained from the imaginary time propagation serving as the initial guess for these dynamical stability studies.

For *case I* In the absence of rotation frequency ($\Omega = 0$), numerically obtained ground state solutions for q2D configuration with the aforementioned coupling for $\gamma_x = 1$ having a vertical stripe pattern in the component densities shown in Fig. 2A and 2C for antiferromagnetic and cyclic phase, respectively. The vertical stripe are emerge due to the effect of SO-coupling $\propto S_x \hat{p}_x$. Fig. 2B and 2D, display the ground state solutions for *case II*, representing horizontal stripe patterns in the antiferromagnetic and triangular-lattice pattern in cyclic phase, respectively, for the aforementioned coupling strength $\gamma = 1$. The nature of the solution would depend on the combined effect of type of interaction, type of SO coupling and strength of SO coupling.

Antiferromagnetic phase

Case I: For the simulation in the rotating frame, we consider different rotation frequencies, $\Omega = 0.5, 0.7$, and 0.9 times the trapping frequency. We select these rotation frequencies to explore all possible vortex lattice configurations that can arise. The anisotropy in the SO coupling leads to a distinction in the angular momentum of the components along the x - and y -directions, thereby impacting the rotational symmetry. Fig. 3(A) illustrates the component densities with a rotation frequency of $\Omega = 0.5$, where a significant portion of the vortices align themselves in a central chain along the x -direction. When considering higher rotation frequencies, such as $\Omega = 0.7$, a larger number of vortices emerge in the system. Some vortices appear on both sides of the central chain, as depicted in Fig. 3(B). The number of vortices in the off-vortices-chain region increases with the rotation frequency. At very large rotation frequency $\Omega = 0.9$ all the vortices arrange themselves on both sides of the central chain, as illustrated in Fig. 3(C). Here, we observed that with strong anisotropic SO coupling and large rotation, some local minima about the trap become discernible, and triangular vortex lattices would preferentially form in the regions outside the vortex chain.

Case II: In the rotating frame, we have observed the evolution of the solution already obtained with ($\Omega = 0$) under various rotation frequencies, $0.5, 0.7$, and 0.9 . Fig. 4(A) illustrates the solution rotated with a frequency of $\Omega = 0.5$. With this relatively low rotation frequency, a small number of vortices have emerged, and all of them tend to arrange themselves in a regular pattern. Fig. 4(B) depicts the vortex lattice structure obtained with a higher rotation frequency of $\Omega = 0.7$. In this case, the central region of the

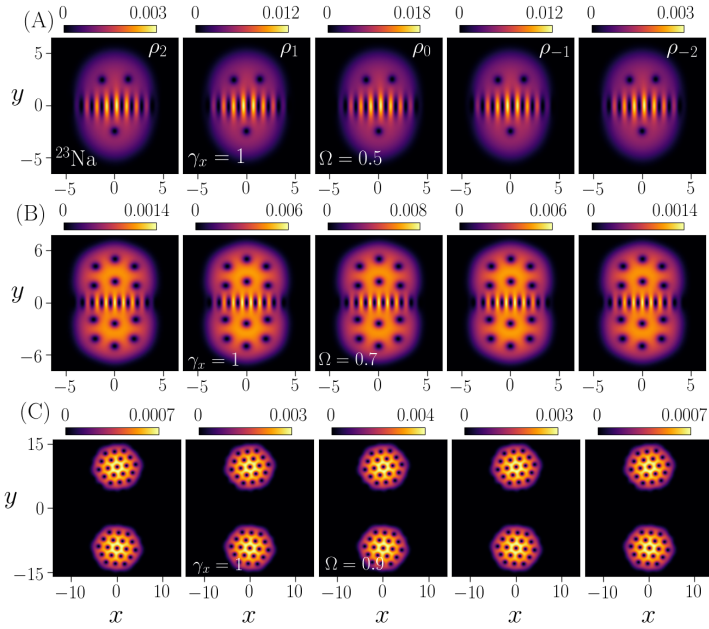


Fig. 3 (Color online) (A) shows the ground state component densities for an anisotropic SO-coupled ^{23}Na spin-2 BEC with $c_0 = 340.45$, $c_1 = 16.90$, $c_2 = -18.25$, $\gamma_x = 1$ with $\Omega = 0.5$. (B) and (C) represent the same for the rotation frequencies $\Omega = 0.7$ and 0.9 , respectively.

structure accommodates singularities with charges $(0, +1, +2, +3, +4)$ in the $(j = -2, -1, 0, +1, +2)$ components, respectively. The charges of these singularities have been determined from the phase of the density profiles (not shown here). As the rotation frequency increases, the number of vortices also increases. Subsequently, we further increased the rotation frequency to $\Omega = 0.9$. At this frequency, we observed the formation of a ring-type structure with a giant vortex located near the center of the trap. And triangular vortex lattices appear in the annular region surrounding the central vortex depicted in Fig. 4(C). The number of vortices within a circle of radius 9.47 is consistent with the number obtained from variational analysis. The variational analysis for this case is showing an excellent agreement particularly at higher rotation frequencies.

Cyclic phase

Case I: The solution reported in Fig. 2(C) evolved in a rotating frame with rotation frequencies of $\Omega = 0.5, 0.7$, and 0.9 . The corresponding results are depicted in Fig. 5(A), (B), and (C), respectively. At a small rotation frequency of $\Omega = 0.5$, the majority of vortices align themselves along a horizontal chain, while the remaining vortices position themselves either above or below this vortex chain. This configuration is illustrated in Fig. 5(A). As the rotation

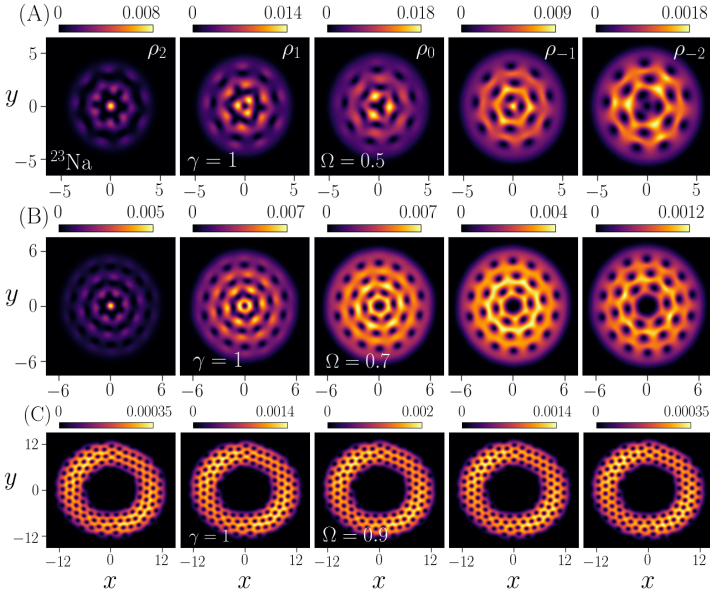


Fig. 4 (Color online) (A) present the component densities of the ground state for an isotropic SO-coupled ^{23}Na spin-2 BEC with $c_0 = 340.45, c_1 = 16.90, c_2 = -18.25, \gamma = 1$ with $\Omega = 0.5$. (B) and (C) showing the same for rotation frequencies $\Omega = 0.5, 0.7$, and 0.9 , respectively.

frequency increases to $\Omega = 0.7$, more vortices emerge in the condensate, as depicted in Fig. 5(B). Finally, at a very high rotation frequency of $\Omega = 0.9$, a large number of vortices are observed, and they arrange themselves in a triangular vortex lattice pattern, as shown in Fig. 5(C).

Case II: Fig. 6(A) illustrate the vortex lattice configuration at $\Omega = 0.5$. In Fig. 6(B), vortex lattice configuration shows corresponding to $\Omega = 0.7$, where the central part of the structure hosting $(0, +1, +2, +3, +4)$ singularities in $(j = -2, -1, 0, +1, +2)$ components. At $\Omega = 0.9$, a vortex lattice structure having a giant vortex at the center and the triangular vortex lattice pattern appear in the annulus as shown in Fig. 6(C).

The rotational energy of a scalar BEC in the rotating frame ($E_\Omega - E_0$) is the energy of rigid-body rotation $-I\Omega^2/2$ where I is the moment of inertia of the condensate [29]. This energy is proportional to the square of the angular frequency [13, 29], where E_Ω is given by Eq. (17). In the case of spin-2 spinor antiferromagnetic and cyclic BECs, also hold a similar relation. We illustrate in Fig. 7 the rotational energy for both antiferromagnetic and cyclic spin-2 BEC for isotropic SO coupling. Here, we plot the energy of the ground state versus Ω . The energies of antiferromagnetic and cyclic systems lie in two separate distinct lines exhibit similar qualitative behavior. As the rotation frequency increases, the energy decreases due to the negative contribution of the rotational energy term $-\Omega L_z$ in the energy expression Eq. (17). This behavior is particularly

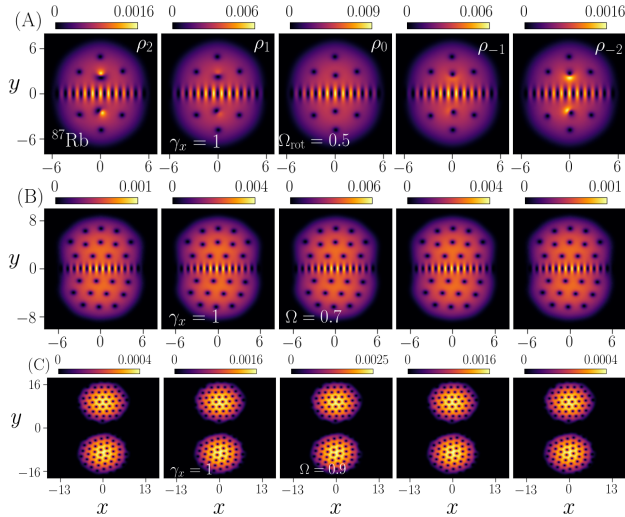


Fig. 5 (Color online) (A) shows the ground state density profiles of the individual components of the SO-coupled ^{87}Rb spin-2 BEC with $c_0 = 1164.80$, $c_1 = 13.88$, $c_2 = 0.43$, anisotropic SO coupling $\gamma_x = 1$, $\Omega = 0.5$. Similarly, (B) and (C) present the component densities for $\Omega = 0.7$ and 0.9 , respectively.

evident in Figure 7, where the rotational energy is behaving $\propto -\Omega^2$ as the rotation frequency increases specially at higher Ω .

Ferromagnetic phase: Here we have considered 50,000 atoms of ^{83}Rb in an SO-coupled spin-2 BEC with or without rotation frequency. The value of three scattering length considered for this system are $a_0 = 83.0a_B$, $a_2 = 82.0a_B$, $a_4 = 81.0a_B$ [19] and corresponding interaction parameters are $(c_0, c_1, c_2) = (980.33, -1.71, 6.86)$. The numerical results obtained for ^{83}Rb under rotation demonstrate qualitative similarities to the cyclic ^{87}Rb BEC. So as we have opted not to include the results obtained for the ferromagnetic case in this work. In the actual parameters magnitude of c_1 and c_2 is very small comparing to c_0 , so at moderate to high rotation frequencies the effect of interaction is negligible compare to Ω . By adjusting the parameters c_1 (more attractive) or c_2 (more repulsive) or both, such that the system's interaction becomes comparable to the rotation frequency, we can effectively study the impact of interaction terms. This will allow us to distinguish between the ferromagnetic and cyclic phases. [16].

5 summary

We have demonstrated the vortex lattice structures in q2D in SO-coupled spin-2 BEC under rotation by employing the variational method for single particle and numerical solution of the mean-field model. In this work, we considered isotropic as well as fully anisotropic SO-coupling strengths with moderate and higher rotation frequencies. In this work, antiferromagnetic ^{23}Na , cyclic phase

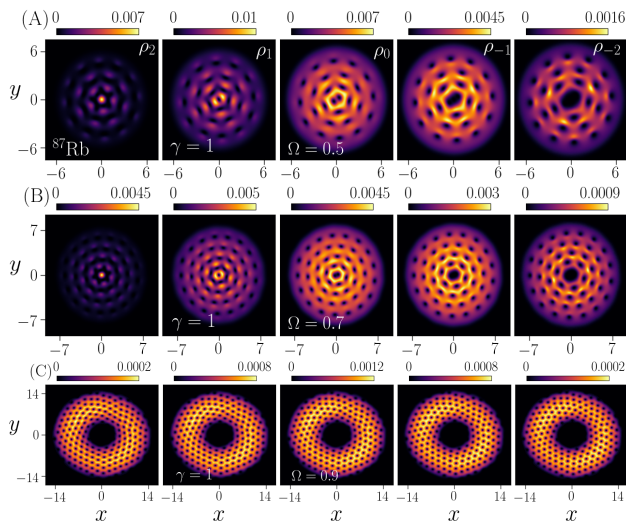


Fig. 6 (Color online) (A) shows the ground state density profiles of the individual components of the SO-coupled ^{87}Rb spin-2 BEC with $c_0 = 1164.80$, $c_1 = 13.88$, $c_2 = 0.43$, isotropic SO coupling $\gamma = 1$, $\Omega = 0.5$. Similarly, (B) and (C) present the component densities for $\Omega = 0.7$ and 0.9 , respectively.

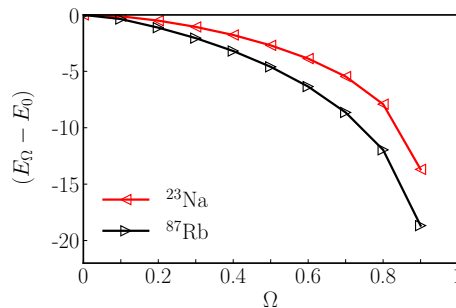


Fig. 7 (Color online) The plot shows the variation of rotational energy ($E_\Omega - E_0$) with the Ω for both antiferromagnetic ^{23}Na and cyclic ^{87}Rb systems.

^{87}Rb and ferromagnetic ^{83}Rb have been discussed in detail. We observed that at fast rotational frequencies, all the phases have qualitatively similar behavior which highlights the negligible role of the spin-exchange interactions. In the presence of anisotropic SO coupling $\gamma_x S_x \hat{p}_x$ bosons experienced symmetric double-well potential, and the central vortices chain appeared along the x -direction in the numerical solutions. Depending on the rotation frequency, the majority of vortices are arranged on both sides of the central chain of vortices. We have reported effective potential curves explored by using single particle Hamiltonian. With isotropic SO coupling $\gamma(S_x \hat{p}_y - S_y \hat{p}_x)$ in the presence of rotation frequency bosons experienced toroidal shape trapping potential, and the radius of the toroidal trap increased with the rotation frequency. So at higher rotation frequency in an isotropic SO-coupled system giant vortex-type

solution observed as a ground state solution. At large rotation, vortices favor triangular vortex lattice patterns in the annual region. All the numerical results reported in this work have been explained by using variational analysis for single particle Hamiltonian.

6 Appendix

The single particle Hamiltonian for case I is

$$H_{\text{rot}} = \left(\frac{\hat{p}_x^2 + \hat{p}_y^2}{2} + \frac{x^2 + y^2}{2} - \Omega L_z \right) \times \mathbb{1} + \gamma_x S_x p_x, \quad (19)$$

Under a unitary transformation the H_{rot} can be diagonalised, which has the eigenvalues

$$E_{\pm 2}(k_x, k_y) = \frac{1}{2} [k_x^2 + k_y^2 \pm 4\gamma_x k_x] - \Omega(xk_y - yk_x), \quad (20a)$$

$$E_{\pm 1}(k_x, k_y) = \frac{1}{2} [k_x^2 + k_y^2 \pm 2\gamma_x k_x] - \Omega(xk_y - yk_x), \quad (20b)$$

$$E_0(k_x, k_y) = \frac{1}{2}(k_x^2 + k_y^2) - \Omega(xk_y - yk_x), \quad (20c)$$

The spectrum in Eqs. (20a)-(20b) around a minima can be described by a parabola of form $(k_x - k_{x\text{min}})^2 + (k_y - k_{y\text{min}})^2 + E_{\text{min}}$, which describes the particle moving in an effective gauge field $(\mathbf{A}, \bar{\Phi}) = (\{k_{x\text{min}}, k_{y\text{min}}, 0\}, E_{\text{min}})$, where \mathbf{A} and $\bar{\Phi}$ are vector and scalar potentials, respectively [6]. In the presence of rotation term $k_{x\text{min}}, k_{y\text{min}}$ and E_{min} become spatially dependent [6]. Rewriting Eqs. (20a)-(20b) as

$$E_{\pm 2}(k_x, k_y) = \frac{1}{2} [(k_x \pm (2\gamma_x \pm y\Omega))^2 + (k_y - x\Omega)^2] + E_{\pm 2}^{\text{min}}(x, y), \quad (21a)$$

$$E_{\pm 1}(k_x, k_y) = \frac{1}{2} [(k_x \pm (\gamma_x \pm y\Omega))^2 + (k_y - x\Omega)^2] + E_{\pm 1}^{\text{min}}(x, y), \quad (21b)$$

$$E_0(k_x, k_y) = \frac{1}{2} ((k_x + y\Omega)^2 + (k_y - x\Omega)^2) + E_0^{\text{min}}(x, y), \quad (21c)$$

where $\mathbf{A}_{\pm 2} = \mp(2\gamma_x \pm y\Omega, x\Omega)$, $\mathbf{A}_{\pm 1} = \mp(\gamma_x \pm y\Omega, x\Omega)$, $\mathbf{A}_0 = (-y\Omega, x\Omega)$, and $\bar{\Phi}_j = E_j^{\text{min}}$ with $(j = 0, \pm 1, \pm 2)$. The effective potentials, which are the sums of trapping and scalar potentials [6], can now be written as

$$V_{\text{eff}}^{\pm 2}(x, y) = \frac{1}{2} [(1 - \Omega^2)(x^2 + y^2) - 4\gamma_x^2 \mp 4y\gamma_x\Omega], \quad (22a)$$

$$V_{\text{eff}}^{\pm 1}(x, y) = \frac{1}{2} [(1 - \Omega^2)(x^2 + y^2) - \gamma_x^2 \mp 2y\gamma_x\Omega], \quad (22b)$$

$$V_{\text{eff}}^0(x, y) = \frac{1}{2} [(1 - \Omega^2)(x^2 + y^2)]. \quad (22c)$$

From Eqs. (22)a - (22)c, the effective potential curves correspond to $V_{\text{eff}}^{\pm 2}$ are the lowest lying depending on the region.

7 Acknowledgement

I thank Sandeep Gautam for the fruitful discussions and comments on the manuscript.

References

- [1] Y.-J. Lin, K. Jiménez-García, and I.B. Spielman, *Nature* **471**, 83 (2011); D.L. Campbell, R.M. Price, A. Putra, A. Valdés-Curiel, D. Trypogeorgos, and I.B. Spielman, *Nature Communications* **7**, 10897 (2016); X. Luo, L. Wu, J. Chen, Q. Guan, K. Gao, Zhi-Fang Xu, L. You, and R. Wang, *Scientific Reports* **6**, 18983 (2016).
- [2] Z.F. Xu, R. Lü, and L. You, *Phys. Rev. A* **83**, 053602 (2011).
- [3] T. Kawakami, T. Mizushima, and K. Machida, *Phys. Rev. A* **84**, 011607(R)(2011); Z. F. Xu, Y. Kawaguchi, L. You, and M. Ueda, *Phys. Rev. A* **86**, 033628 (2012).
- [4] B. M. Anderson, I. B. Spielman, and G. Juzeliūnas, *Phys. Rev. Lett.* **111**, 125301 (2013); Z.-F. Xu, L. You, and M. Ueda, *Phys. Rev. Rev. A* **87**, 063634 (2013).
- [5] X.-Q. Xu and J. H. Han, *Phys. Rev. Lett.* **107**, 200401 (2011).
- [6] J. Radić, T. A. Sedrakyan, I. B. Spielman, and V. Galitski, *Phys. Rev. A* **84**, 063604 (2011); J. Radić, *Spin-orbit-coupled quantum gases* (2015) [Doctoral dissertation, Maryland University].
- [7] X.-F. Zhou, J. Zhou, and C. Wu, *Phys. Rev. A* **84**, 063624 (2011).
- [8] C.-F. Liu, H. Fan, Y.-C. Zhang, D.-S. Wang, and W.-M. Liu, *Phys. Rev. A* **86**, 053616 (2012).
- [9] A. Aftalion and P. Mason, *Phys. Rev. A* **88**, 023610 (2013).
- [10] H. Wang, L. Wen, H. Yang, C. Shi, and J. Li, *J. Phys. B: At. Mol. Opt. Phys.* **50**, 155301 (2017). C. Shi, L. Wen, Q. Wang, H. Yang, and H. Wang, *J. Phys. Soc. Jpn.* **87**, 094003 (2018); H. Yang, Q. Wang, N. Su,

- and L. Wen, Eur. Phys. J. Plus, **134**, 589 (2019); Q.-B. Wang, H. Yang, N. Su, and L.-H. Wen, Chin. Phys. B **29**, 116701 (2020); J.-G. Wang and Y.-Q. Li, Results in Physics **17**, 103099 (2020).
- [11] C.-F. Liu, Y.-M. Yu, S.-C. Gou, and W.-M. Liu, Phys. Rev. A. **87**, 063630 (2013).
- [12] Q. Zhao and H. Bi, Int. J. Theor. Phys. **60**, 2778 (2021).
- [13] S. K. Adhikari, J. Phys.: Condens. Matter **33**, 065404 (2021).
- [14] P. Peng, G.-Q. Li, W.-L. Yang, and Z.-Y. Yanga, Phys. Lett. A **382**, 2493 (2018); X.-F. Zhang, B. Li, and S.-G. Zhang, Laser Phys. **23**, 105501 (2013).
- [15] J. Li, X.-F. Zhang, and W.-M. Liu, ,Ann. Phys. **87** 396 (2018).
- [16] P. Banger, R K. Kumar, A. Roy, and S. Gautam, J. Phys.: Condens. Matter **35**, 045401 (2023).
- [17] G.-P. Chen, P. Tu, C.-B. Qiao, J.-X. Zhu, Q. Jia, and X.-F. Zhang, Frontiers in Physics, **9**, 613 (2021).
- [18] H. Zhu, C.-F. Liu, D.-S. Wang, S.-G. Yin, L. Zhuang, and W.-M. Liu, Phys. Rev. A **104**, 053325 (2021).
- [19] C V. Ciobanu, S. Yip, T. Ho, Phys. Rev. A **61** (2000) 033607.
- [20] A. Widera, F. Gerbier, S. Fölling, T. Gericke, O. Tatjana and I. Bloch, New Journal of Physics **8** (2006) 152.
- [21] Y. Kawaguchi, M. Ueda, Physics Reports **520** (2012) 253-381.
- [22] N. Goldman, G Juzeliūnas, P. Öhberg, and I. B. Spielman, Rep. Prog. Phys. **77**, 126401 (2014).
- [23] I. E. Rashba and Y. A. Bychkov Journal of Physics C **17**, 6039 (1984).
- [24] P. Kaur, A. Roy, and S. Gautam, Comp. Phys. Comm. **259**, 107671 (2021)
- [25] P. Banger, P. Kaur, S. Gautam, Int. J. Mod. Phys. C **33**(4), 2250046 (2022).
- [26] R. Ravisankar, D. Vudragović, P. Muruganandam, A. Balaž, and S. K. Adhikari, Comp. Phys. Comm. **259**, 107657 (2021); P. Muruganandam, A. Balaž , and S. K. Adhikari, Comp. Phys. Comm. **264**, 107926 (2021).

- [27] P. Banger, P. Kaur, A. Roy, and S. Gautam, *Comp. Phys. Comm.* **279**, 108442 (2022).
- [28] P. Kaur, S. Gautam, S.K. Adhikari, *Phys. Rev. A*, **105**, 023303 (2022).
- [29] AL. Fetter, *Rev. Mod. Phys.* **81** (2009) 647.